

PAPER

Molecular breast tomosynthesis with scanning focus multi-pinhole cameras

To cite this article: Jarno van Roosmalen *et al* 2016 *Phys. Med. Biol.* **61** 5508

View the [article online](#) for updates and enhancements.

Related content

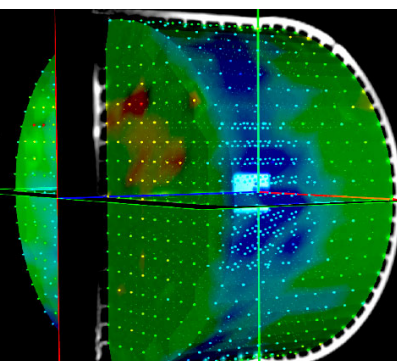
- [Comparison of fan beam, slit-slat and multi-pinhole collimators for molecular breast tomosynthesis](#)
Jarno van Roosmalen, Freek J Beekman and Marlies C Goorden
- [System geometry optimization for molecular breast tomosynthesis with focusing multi-pinhole collimators](#)
Jarno van Roosmalen, Freek J Beekman and Marlies C Goorden
- [Voxelized ray-tracing simulation dedicated to multi-pinhole molecular breast tomosynthesis](#)
Beien Wang, Jarno van Roosmalen, Louis Piët *et al.*


Recent citations

- [Characterization of a multi-pinhole molecular breast tomosynthesis scanner](#)
Beien Wang *et al*
- [Primary, scatter, and penetration characterizations of parallel-hole and pinhole collimators for I-123 SPECT](#)
Arda Könik *et al*
- [Evaluation of pinhole collimator materials for micron-resolution *ex vivo* SPECT](#)
Minh Phuong Nguyen *et al*

**LIGHTER, LARGER with
SUB-MILLIMETER ACCURACY**

Quantify MRI Geometric
Distortion in **3D**





MRID^{3D}

Molecular breast tomosynthesis with scanning focus multi-pinhole cameras

Jarno van Roosmalen¹, Marlies C Goorden¹
and Freek J Beekman^{1,2}

¹ Section Radiation, Detection & Medical Imaging, Delft University of Technology,
Delft, The Netherlands

² MILabs B.V., Utrecht, The Netherlands

E-mail: j.vanroosmalen@tudelft.nl

Received 8 April 2016

Accepted for publication 13 June 2016

Published 6 July 2016



Abstract

Planar molecular breast imaging (MBI) is rapidly gaining in popularity in diagnostic oncology. To add 3D capabilities, we introduce a novel molecular breast tomosynthesis (MBT) scanner concept based on multi-pinhole collimation. In our design, the patient lies prone with the pendant breast lightly compressed between transparent plates. Integrated webcams view the breast through these plates and allow the operator to designate the scan volume (e.g. a whole breast or a suspected region). The breast is then scanned by translating focusing multi-pinhole plates and NaI(Tl) gamma detectors together in a sequence that optimizes count yield from the volume-of-interest. With simulations, we compared MBT with existing planar MBI. In a breast phantom containing different lesions, MBT improved tumour-to-background contrast-to-noise ratio (CNR) over planar MBI by 12% and 111% for 4.0 and 6.0 mm lesions respectively in case of whole breast scanning. For the same lesions, much larger CNR improvements of 92% and 241% over planar MBI were found in a scan that focused on a breast region containing several lesions. MBT resolved 3.0 mm rods in a Derenzo resolution phantom in the transverse plane compared to 2.5 mm rods distinguished by planar MBI. While planar MBI cannot provide depth information, MBT offered 4.0 mm depth resolution. Our simulations indicate that besides offering 3D localization of increased tracer uptake, multi-pinhole MBT can significantly increase tumour-to-background CNR compared to planar MBI. These properties could be promising for better estimating the position, extend and shape of lesions and distinguishing between single and multiple lesions.

Keywords: breast imaging, pinholes, tomosynthesis, SPECT

 Online supplementary data available from stacks.iop.org/PMB/61/5508/mmedia

(Some figures may appear in colour only in the online journal)

1. Introduction

Mammography is currently the most frequently used imaging modality in breast cancer screening, as it allows for performing fast, high-resolution, and relatively low-dose imaging of the breast. Nevertheless, mammography has its limitations; it is widely recognized that for women with radiographically dense breasts, the sensitivity and specificity of mammography are significantly reduced (Kolb *et al* 2002, Carney *et al* 2003, Pisano *et al* 2008). Therefore, other modalities such as ultrasound imaging, x-ray tomosynthesis, Magnetic Resonance Imaging, Positron Emission Tomography, molecular breast imaging (MBI) and single photon emission computed tomography (SPECT) are actively being investigated to complement or replace mammography for some groups of patients (Harris 2010, Lee *et al* 2010). For a comprehensive review of the different breast imaging modalities we refer to Hruska and O'Connor (2013) and Fowler (2014).

Different imaging modalities can provide complementary types of information. Functional nuclear imaging techniques, which visualize uptake of radiolabelled molecules have the ability to visualize the physiology of breast tissue opposed to just its anatomic appearance. Therefore, these techniques cannot solely detect tumours, but they may also reveal specific characteristics of the cancer and indicate possible response to therapy, or be used for therapy follow-up (Mankoff *et al* 2007). Benefits of functional techniques are widely recognized as shown by the recent development of dedicated breast PET systems (Miyake *et al* 2014) and several dedicated planar breast imaging systems for single photon emitting tracers. These planar systems are known under a wide range of names such as Breast Specific Gamma Imaging, MBI and, mammoscintigraphy (Brem *et al* 2008, O'Connor *et al* 2008, Hruska *et al* 2012b, Dickerscheid *et al* 2013, Sun *et al* 2013). We will here collectively refer to them as planar MBI. Planar MBI was initially developed as an alternative imaging modality for specific patient groups, like women with dense breasts (O'Connor *et al* 2007). Recently, there has been a very active development in planar MBI instrumentation, resulting in strong sensitivity improvements. This enabled the use of a lower dose, which may open up the possibility for using MBI in breast cancer screening.

Planar (2D) breast imaging has the disadvantage that it does not provide information on the depth of a suspect lesion and that malignant features may be obscured by overlapping breast tissue. As an extension to 2D mammography, x-ray tomosynthesis (which adds 3D information to mammography) is currently growing in popularity (Sechopoulos 2013) as several screening studies demonstrated improved lesion detection and reduced recall rates of x-ray tomosynthesis over mammography (Skaane *et al* 2013, Lång *et al* 2016). Given these results, it may be worthwhile to explore similar extensions for planar MBI. Besides providing 3D tumour localization, 3D information may allow discriminating between a large tumour and several small ones close together and enable better estimation of its size and shape. Several groups have already attempted 3D imaging of single photon emitting tracers in breasts using dedicated SPECT or molecular tomosynthesis systems (Madhav *et al* 2006, Williams *et al* 2010, Perez *et al* 2011, Gopan *et al* 2014, Gong and Williams 2015). However, compared to recent planar systems, the sensitivity-resolution trade-offs of these scanners are still sub-optimal, mainly due to the relatively large distance between breast and detector.

One way to achieve 3D MBI with high resolution and sensitivity could be by utilizing and adapting techniques from the field of preclinical SPECT which has seen much innovation and progress in the past decade (Peterson and Furenlid 2011, Peterson and Shokouhi 2012). Modern small animal SPECT commonly uses pinhole collimators to project the tracer distributions onto the gamma detectors. To obtain high-count yields from a specific volume-of-interest (VOI), such as an organ or tumour, one can use focusing multi-pinhole geometries (Beekman and van der Have 2007, van der Have *et al* 2009). In this class of scanners, the user can designate a specific scan volume, e.g. by using a graphical user interface based on optical cameras that view the subject. The subject is then stepped in a specific sequence through the scanner in order to optimize the count yield from the VOI. Such focusing multi-pinhole collimators may also be well suited for high resolution and high sensitivity imaging of breast tumours (Branderhorst *et al* 2011, 2014), while maintaining excellent capabilities for imaging the entire breast.

In this work, we explore the use of a focusing multi-pinhole geometry for 3D breast imaging. The design is based on two multi-pinhole plates acting as collimators that are placed in close proximity to a lightly compressed breast. With this geometry, data is acquired over a limited range of angles similar to x-ray tomosynthesis. The breast is viewed through transparent compression plates by webcams, which allow the user to select the VOI to be scanned on a graphical interface. The aim of this paper is to present and evaluate this novel dedicated molecular breast tomosynthesis (MBT) scanner design. With simulations, we (i) compare MBT's performance with recently developed planar MBI, (ii) evaluate the ability to collect depth information for tumour detection, and (iii) investigate if and how much MBT scans are improved by focusing on a VOI instead of imaging the whole breast.

2. Methods

In this section, we describe the novel MBT design as well as the planar MBI camera that it is compared with. Additionally, details of the digital phantoms used and simulations performed are provided.

2.1. MBT scanner design

In the MBT scanner proposed in this paper, the patient lies prone on a specially designed bed (figure 1(a)) that has an opening for the breast. To also allow imaging of breast tissue close to the chest wall, the pendant breast should hang as deep as possible in the adjustable slit formed by two L-shaped round-edged transparent Perspex plates underneath the bed (see figure 2) (Beekman 2011, 2014). These plates lightly compress the pendant breast. We assume similar levels of compression as reported for planar MBI (Hruska *et al* 2008), which is much less than the compression used in mammography. This improves patient comfort, which is required as in radiotracer-based breast imaging patients typically will have to endure a 10–20 min scan. Some level of compression is preferred as it prevents motion during a scan and it reduces the thickness of the breast, which is beneficial for sensitivity, as the collimators can be placed closer to the breast's tissue.

The whole imaging set-up underneath the bed can be rotated (see figure 1(b)) between scans. Thus, it allows for compressing the breast under similar view angles and breast deformation as used in x-ray mammography and planar MBI, i.e. the CC view and the MLO view. By summing the acquired 3D images along the appropriate direction, comparable 2D images can be generated. Consecutive image acquisitions for different orientations of course require



Figure 1. Patient table and compression for the proposed MBT scanner. (a) A woman lying prone on the scanner table with one breast in the opening in the bed. (b) Schematic representation of the compression in the scanner. As shown, the breast can be imaged in different views analogous to the craniocaudal (CC) and mediolateral oblique (MLO) views in mammography. (c) The patient is laying on her side and fully extending her arm downward between the compression plates which allows for scanning the right armpit. (d) Schematic representation of imaging the armpit.

re-compressing the breast in another position, as one also has to do for planar MBI or mammography. A prototype patient bed was evaluated with a group of 10 women, and, no problems with placing of the shoulders and arms were found, as their position was the same for MLO compression as for CC compression.

Although this paper focuses on breast imaging capabilities of MBT, an additional feature of this flexible setup is that it might also allow scanning of the armpit by having the patients lie on their side and move their arm downwards, see figures 1(c) and (d). However, the capabilities for the latter application would have to be investigated during a separate study.

Optical cameras view the compressed breast through the transparent compression plates (see figure 2(a)). With a graphical user interface, the user can then designate the volume to be scanned, which can e.g. be the whole breast, a suspected region, or a known tumour. Targeted imaging based on scan planning with optical cameras is already in use in preclinical SPECT and it has been shown that focusing on a VOI leads to increased count yields from the VOI (Branderhorst *et al* 2011). This can result in improved contrast-to-noise trade-offs or offer the possibility of reduced acquisition time or lower tracer dose.

After volume selection, two collimator-detector combinations, which are positioned below the patient bed, move into the scanning position (figure 2(b)). During scanning, these

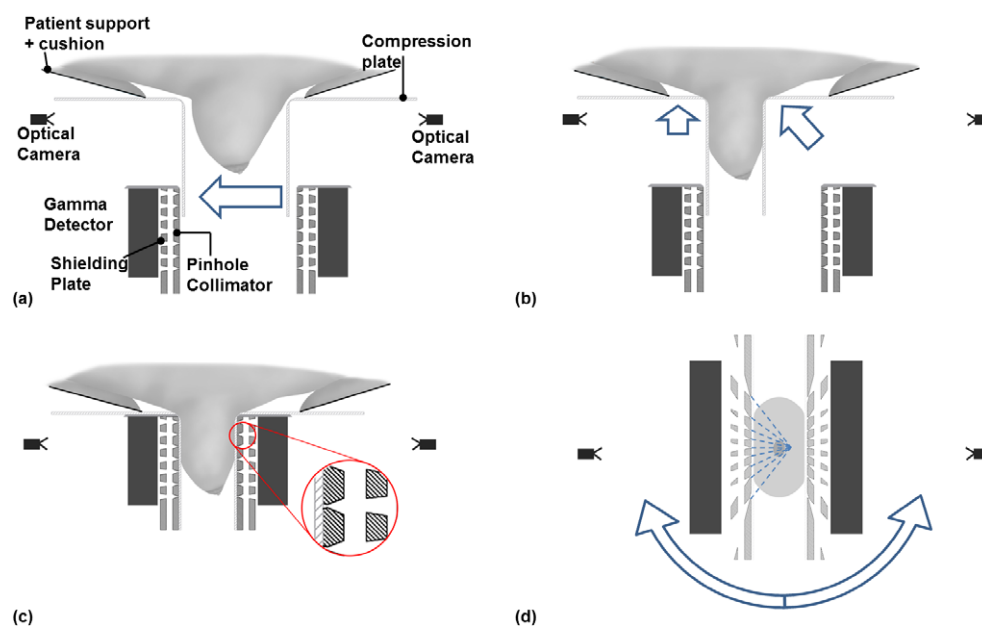


Figure 2. The compression process and scanner geometry: (a) transparent plates compress the breast (artist impression) and a VOI is selected using optical cameras. (b) After scan volume selection, the collimator plates and gamma detectors move into scanning position (arrows). (c) Collimator and gamma detector in scanning position, with inset showing collimator detail. (d) Perpendicular cross-section through collimator-gamma detector set-up showing the pinhole geometry. Dashed lines indicate the pinhole axes, which converge on a line 40 mm from the collimator. Arrows indicate rotation of whole scanner-head to enable different views.

gamma detectors and collimators translate and in this way acquire gamma-ray projections of the compressed breast in different positions. Collimator and gamma detector designs are described below as well as the sequence of positions used.

2.1.1. MBT multi-pinhole collimator. Collimation of the gamma photons emitted by the tracer is achieved by using two 10 mm thick tungsten collimator plates each containing 63 pinholes that all ‘see’ part of the breast and project onto one of the two gamma detectors which are placed 3.6 cm from the compression plates (12 mm thickness) (see figures 2(c) and (d)). The pinhole axes in each collimator plate are directed towards a focus line 40 mm from the collimator face; see figure 2(d) in which pinhole axes are drawn for one of the collimator plates. The knife-edge pinholes have a diameter of 2.7 mm and an opening angle of 42 degrees. Overlapping projections on the gamma camera can cause image artefacts, e.g. Vunckx *et al* (2008) and Mok *et al* (2009). Therefore, projections from different pinholes are prevented from overlapping by a tungsten shielding plate, which is placed in between the collimator and detector, similar to the shielding tube introduced in Beekman *et al* (2005). This shielding plate contains rectangular holes and has a thickness of 12 mm. The pinholes and the corresponding holes in the shielding plate are positioned such that the projections on the detector from different pinholes are adjacent with a 3 mm separation between them (see figure A1 in the supplementary information) (stacks.iop.org/PMB/61/5508/mmedia). The distance between the pinholes in the sagittal view (figure 3) is 23.9 mm, while in the coronal view the

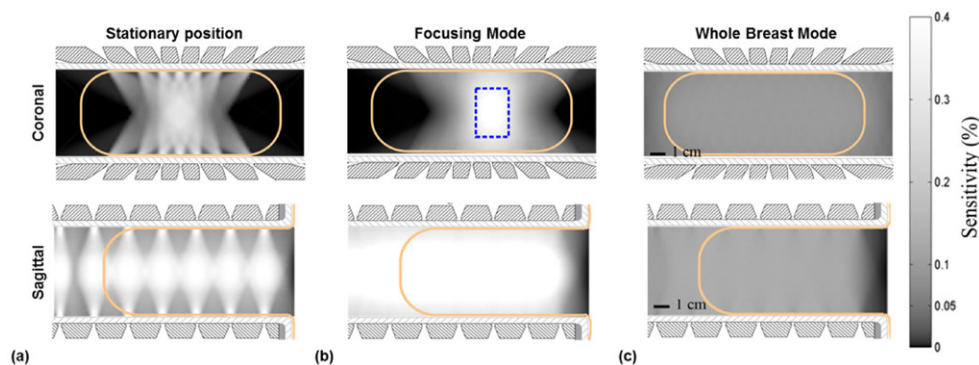


Figure 3. Maps of the sensitivity in the FOV of the system. Top row represents sensitivity in a cross section along the coronal plane, bottom row along the sagittal plane. Maps represent (a) a single stationary collimator position, (b) the focusing mode (FM) and (c) the whole breast mode (WBM). Solid orange contour lines indicate the size of an average breast, blue dashed rectangle is the area for which sensitivity in the FM is reported in section 3.

distance varies from 13.3 to 38 mm. The combined thickness of collimator and shielding plate provides sufficient stopping power for imaging tracers based on $^{99\text{m}}\text{Tc}$ and ^{123}I (e.g. for $^{99\text{m}}\text{Tc}$ a fraction of $6 \cdot 10^{-33}$ is transmitted).

Tomographic imaging requires sufficient angular sampling of the data to be able to guarantee good reconstructions. In breast imaging, it is very hard to simultaneously obtain complete sampling and place the collimator close to the breast, the latter being highly desirable for obtaining high sensitivities with pinhole collimators and high resolutions with pinhole and parallel hole collimators. In our system, the arrangement of the pinholes in two collimator plates means that the pinholes do not cover a full 180-degree range, as is required for data completeness (Orlov 1975, Tuy 1983). Consequently, we expect the resolution parallel to our detectors to be higher than the resolution in the perpendicular direction. This resembles the way x-ray tomosynthesis adds 3D information to mammography, without achieving the full 3D capability of x-ray computed tomography. Therefore, we use the term MBT to describe our scanner, instead of breast SPECT.

2.1.2. MBT detector. In this simulation study, we evaluated the use of a conventional PMT-based scintillation detector employing a continuous NaI(Tl) crystal. In contrast, cadmium zinc telluride (CZT) detectors are often selected for planar MBI because they can provide better spatial and energy resolutions than continuous NaI(Tl) coupled to an array of PMTs. However, compared to planar MBI, system resolution in a pinhole-geometry such as used in MBT is not limited by the intrinsic detector resolution because pinholes can generate magnified projections of the activity distribution on the detector. Thus, image resolutions far better than the detector resolution can be obtained; e.g. small-animal systems can obtain 0.25 mm image resolution using conventional detectors with only 3.2 mm intrinsic detector resolution (Ivashchenko *et al* 2014). Standard available CZT detectors offer lower detection efficiency than NaI(Tl) and initial calculations of system resolution and sensitivity of different MBT designs with CZT or NaI(Tl) detectors have shown that for the MBT design proposed here the higher spatial resolution of CZT detector does not outweigh the loss in efficiency (van Roosmalen *et al* 2015). The higher energy resolution of CZT compared to NaI(Tl) can be advantageous

for scatter rejection although some studies indicate that scatter might not be a significant issue for this type of geometry as we discuss in more detail in section 2.5.1. As a conventional PMT-based NaI(Tl) gamma detector is also available at much lower costs than CZT detectors, we prefer this type of detector for our design.

For our detectors, we assumed an active area of $25 \times 15 \text{ cm}^2$ and a scintillator thickness of 9.5 mm for each detector, which is read out by an array of 2-inch PMTs. For breast imaging, it is important and challenging to image also breast tissue close to the chest wall. This sets strong requirements on the allowed dead area near the detector's edge. Barrett *et al* (2009) have used Maximum Likelihood processing of the PMT signals (Milster *et al* 1990, Moore *et al* 2007, Barrett *et al* 2009), instead of standard Anger logic. They showed that it is possible to reduce dead edge effects for NaI(Tl) detector. Based on their results, we assume a total dead edge of 5 mm, which includes shielding/housing of the crystal. An intrinsic detector resolution of 3.2 mm was assumed which can be attained with Anger logic already. The detector efficiency was assumed to be 90%, corresponding to the stopping power of 9.5 mm NaI(Tl) for 140 keV gamma photons ($^{99\text{m}}\text{Tc}$).

2.2. Movement and scanning modes

The focused collimator design presented here provides users of the MBT scanner with the unique ability of having the freedom to perform different scans by focusing on a volume of choice. Focusing on a VOI is beneficial because this way the count yield from the VOI can be increased (Branderhorst *et al* 2011). The slices shown in figure 3(a) illustrate which part of the breast is 'seen' by the pinholes when detectors and collimators are in a single stationary position. To image a user-selected volume, the field-of-view (FOV) has to be translated over the breast such that the whole scan volume is viewed over a range of angles (Vastenhouw and Beekman 2007, Vaissier *et al* 2012). This FOV translation is done by synchronized step-and-shoot movement of the collimators and detectors. The sagittal slice in figure 3(a) shows that the FOV contains areas with low sensitivity in between the pinholes. Therefore, the collimators and detectors always have to move in the anterior direction to cover these gaps. The amount of movement depends on breast size but is independent of the size of the VOI. Additionally, collimators and detectors move to the left and to the right (from the patient's reference frame), parallel to the breast. The sequence of steps in horizontal direction depends on the selected VOI. The goal is to design a scan sequence that optimizes count yield from the VOI while simultaneously obtaining a reasonably uniform sensitivity in the whole VOI. The specific scan sequences used in this paper are provided below in section 2.5.2 that describes the phantom experiments.

The movement of collimators and detectors does not only increase the size of the FOV, but also increases the number of angles that sample a point in the FOV. We take all available information into account, as the projection data from all positions is used simultaneously for reconstruction, instead of stitching local reconstructions (Vastenhouw and Beekman 2007).

To compare how different types of scans perform, we will test two different scan modes in this paper. First, the WBM is e.g. for the situation in which the presence of lesions or their location is not known and the whole breast has to be scanned to search for them. Secondly, a FM scan sequence in which one focuses on a smaller region of the breast containing tumours is evaluated. Such a scan may be performed when it is expected that a tumour is present at a certain location and one wants to obtain as detailed as possible its characteristics, e.g. exact shape, activity uptake, etc.

2.3. Planar MBI system

We compare performance of our dedicated MBT scanner with planar MBI. A geometry based on the planar MBI scanner developed by Hruska *et al* (2012a, 2012b) is simulated in this paper. We selected this system as our benchmark, as it has had considerable development and optimisation, thereby making it a good reference for what is currently possible with planar MBI. Furthermore, this system can be used with a similar compression of the breast as our design, allowing for a relatively straightforward comparison.

The simulated planar MBI system employs a pixelated CZT detector of $20 \times 16 \text{ cm}^2$ with 1.6 mm pixels. The tungsten parallel hole collimator is registered to this detector, meaning that each hole of the collimator corresponds to exactly one detector pixel. The square holes have a length of 9.4 mm, a side-length of 1.225 mm and the septal thickness is 0.375 mm.

2.4. Phantom scans

We evaluated the systems' performance on two different phantoms. First, a resolution phantom is used to assess the smallest details that can be resolved. Second, we show simulated images of an anthropomorphic breast shaped phantom containing several lesions to evaluate characteristics for tumour imaging.

2.4.1. Resolution phantom. To determine resolution of MBT, a Derenzo resolution phantom was simulated. The phantom had 6 sectors with rods of 2.0, 2.5, 3.0, 3.5, 4.0, and 4.5 mm diameter (see figure 5(a)). The distance between rods was twice the rod diameter, and the length was 40 mm. The rods contained an activity concentration of 37 kBq ml^{-1} . We did not assume any activity in the background, but did incorporate attenuation in a breast shaped region (see below for the breast phantom). A linear attenuation coefficient of 0.0151 mm^{-1} was assumed which is valid for 140 keV photons in water.

We performed two different simulations, both of 10 min scans but with different phantom orientations. In the first simulated scan, the phantom was placed such that the rods are perpendicular to the transverse plane. The second scan had the rods in a direction perpendicular to the coronal plane. These positions were chosen to determine resolution both in the plane parallel to the detectors as in the plane perpendicular to them (i.e. how accurate is the depth information). We sampled the phantom on a 0.375 mm voxel grid to simulate projections. For MBT we reconstructed the phantom on a 0.75 mm grid using 20 iterations of MLEM as explained below. Note that for planar MBI the projections are used directly and no reconstruction is required. The images are shown unfiltered.

2.4.2. Breast phantom. As our set-up uses moderate compression of the breast, the breast can be modelled quite well as half an elliptically shaped disk (Dong *et al* 2011). Approximating an averagely sized breast, a 110 mm chest-to-nipple distance, a width of 150 mm, and a thickness of 55 mm were set in accordance with results from other breast scans with similar compression (Scopinaro *et al* 1999, Rhodes *et al* 2005, O'Connor *et al* 2007, 2008, Hruska *et al* 2008, Weinmann *et al* 2009), and slightly thicker than often found in mammography literature, in which much more compression is used (Sullivan *et al* 1991, Helvie *et al* 1994).

To assess how differently sized lesions are imaged, we placed four sets with three lesions each in the phantom. Each set has different lesion sizes (4.0, 4.5, 5.0 and 6.0 mm), see figure 4, which shows 2 slices through the phantom. Within each set, the central lesion was placed at a depth of 22 mm, with the other two lesions at a depth of 33 mm, making a triangular

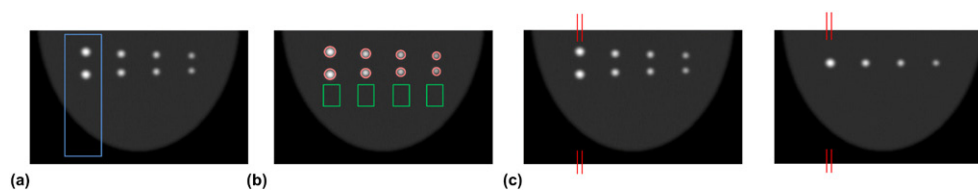


Figure 4. Slices through the breast phantom with regions used in analysis indicated. (a) Region used in FM for imaging largest spheres. (b) Red circles are regions for contrast and CNR calculation, green boxes are background regions for the same. (c) Lines indicate location of profiles shown in figure 8.

arrangement. This is done to test the ability of MBT to differentiate between lesions at different depths. The phantom was sampled on a 0.75 mm voxel grid (and reconstructed on 1.5 mm grid for MBT as explained below).

We assumed a background activity concentration of 3.7 kBq ml^{-1} , consistent with an injection of 925 MBq $^{99\text{m}}\text{Tc}$ -Sestamibi as experimentally determined by Mann *et al* (2012) and consistent with count levels from Hruska *et al* (2012a). We assume a concentration of 37 kBq ml^{-1} in the lesions to give an tumour-background uptake ratio of 10:1, as found in common practise (Maublant *et al* 1996, Lee *et al* 2004, Hruska and O'Connor 2008b, Sullivan *et al* 2012). Again, we simulated 10 min acquisition time.

2.5. Simulations and image reconstruction

In this subsection, we describe the simulation methods used, for both MBT and planar MBI, as well as the way of analysing the results.

2.5.1. MBT. To simulate images that can be obtained by MBT, we developed a ray tracing simulator that calculates the probability that a gamma photon emitted from a certain volume element (voxel) in the breast is detected in a certain detector pixel. This simulator uses the collimator modelled as a voxelized volume (with a voxel size of 0.0625 mm) as its input, where each voxel contains either air or tungsten. The ray tracer calculates the collimator attenuation by determining the amount of collimator material encountered by a gamma photon for each voxel-pixel combination. A threshold was used to ignore small contributions (gamma photons that had a chance of less than the threshold to pass through the collimator were ignored). The depth-of-interaction in the scintillator crystal is modelled by also raytracing the gamma photon through the scintillator, similarly as was described in (Goorden *et al* 2016). Consequently, the detector efficiency of 90% is automatically taken into account. The intrinsic detector resolution was incorporated by modelling detector response with a 3.2 mm FWHM Gaussian. We assumed detector pixels of 1.072 mm in a 234×140 -pixel grid.

To calculate phantom projections, we represented the phantoms on a regular voxel grid (voxel size was mentioned for each phantom in section 2.4). With the raytracer set to a threshold of 1%, we generated simulated projections from the phantoms for each of the positions in the scan sequence. Hereby, we accounted for the activity concentration in the phantom and the scanning time in each position. Moreover, the attenuation in the phantom was modelled using a uniform attenuation coefficient of 0.0151 mm^{-1} valid for 140 keV photons in water. Poisson distributed noise was added to each projection to take into account counting statistics. As mentioned in section 2.1.2, earlier phantom studies for a similar geometry showed that scatter from the torso is not a significant problem (Wang *et al* 1996,

Hruska and O'Connor 2006). This is because gamma photons coming from the torso can only end up on the detector if they scatter over a large angle. As large-angle scattering is associated with a relatively large energy loss, the scattered photons can be identified relatively easy with energy selection. To validate if this was indeed the case for our proposed geometry, we performed simulations with the well-known Monte Carlo package GATE (Jan *et al* 2004, 2011) using the realistic MCAT phantom (Segars and Tsui 2009, Segars *et al* 2010) and activity concentrations found in literature (Wackers *et al* 1989, Wang *et al* 1996, Hruska and O'Connor 2008a, Perez *et al* 2010). These simulations (Wang *et al* 2016) predict that the scatter fraction from the heart and torso in the photopeak (assuming 10% energy resolution and a photopeak window width of 20%) is less than 1.5%, in agreement with the experimental results from (Wang *et al* 1996, Hruska and O'Connor 2006). Therefore, the use of a raytracer that models attenuation but ignores scatter is justified for this geometry.

For the tomographic reconstruction of the projection data, we used the maximum likelihood expectation maximization (MLEM) algorithm. The system matrix used in MLEM was calculated with the same ray tracer as used for the projections but with a threshold of 2% (of the not-attenuated probability of detection) and at a two times coarser voxel size than that used to calculate projections. The discrepancy in voxel size and cut off thresholds between phantom projections and system matrix is to mimic a continuous activity distribution without having an actual threshold on gamma photon transport. We did not use a subset-based acceleration scheme because we found that the lack of complete angular sampling resulted in artefacts even for a small number of subsets. Moreover, we did not use attenuation correction, as the method for obtaining highly accurate information of the breast contour is not yet established. With these settings, a single MLEM iteration takes about 5 min using 6 threads on a AMD Opteron 6344 at 2.6 GHz.

2.5.2. Scan sequences for MBT. As explained in section 2.2, the choice of scan sequence can significantly impact reconstructed images. The sequences used for this study were optimized to yield a uniform sensitivity over the scan area. This was done by translating the sensitivity map from figure 3(a) according to each scan position in the sequence and then calculating an average sensitivity over all scan positions. This results in an estimated sensitivity map for the scan sequence as a whole. In general, increasing the number of steps and thereby reducing the distance between the steps improves the uniformity. Several scan sequences with different amounts of positions were tested. We chose a sequence with the requirement that the 1st percentile of voxels had a sensitivity of at least 10% of the mean sensitivity. From all sequences that fulfilled this requirement, we chose the one that used the lowest amount of positions. The sensitivity of the 1st percentile was used as metric instead of e.g. the standard deviation as even small areas with very low sensitivity can cause image artefacts without showing in the standard deviation of the sensitivity if the rest is smooth enough. Moreover, our software currently requires the step-size to be an integer multiple of the voxel size used during reconstruction.

We evaluate the use of two different sequences, a WBM and a FM. For both modes, we use the same number of steps in the anterior direction. Given the averagely sized breast assumed in this paper (see section 2.4.2), the movement in the anterior direction is done in 10 overlapping steps. The positions for each of these steps are 0.0, 1.5, 4.5, 6.0, 9.0, 10.5, 13.5, 15.0, 18.0 and 19.5 mm, where 0.0 denotes the initial position, which is as close as possible to the chest.

For the left-right movement in WBM, we use a slightly different set of positions for each alternating row (i.e. steps in the anterior direction). This helps to get a uniform coverage of the

breast, while keeping the number of positions low, which reduces the overhead time associated with each movement. The positions are

$$\begin{cases} -75, -66, -57, -48, -39, -30, -21, -12, -3, 6, 15, 24, 33, 42, 51, 60, \text{ and} \\ 69 \text{ mm, for even rows} \\ -69, -60, -51, -42, -33, -24, -15, -6, 3, 12, 21, 30, 39, 48, 57, 66, \text{ and} \\ 75 \text{ mm, for odd rows,} \end{cases}$$

with 0 denoting the position with the collimator centred over the breast. In FM, the horizontal movement of collimator and detector is given with respect to the centre of the VOI. For the VOI setting used in our simulations (see figure 4(a) and section 2.4.2), the positions are given by -9.0 , -6.0 , -3.0 , -1.5 , 1.5 , 3.0 , 6.0 , and 9.0 mm.

Data from the resolution phantom was acquired with the WBM, while for the breast phantom both modes were tested.

2.5.3. Planar MBI. We simulated the planar MBI system using the same ray tracing software as used for the MBT scanner. The voxelized collimator model (with 0.025 mm voxels) used in this software was carefully aligned with the detector to match the holes to the detector pixels. We did not assume detector blurring, as the simulated system uses a pixelated detector design. The planar scanner directly produces an image instead of projections that serve as input to a reconstruction algorithm. Therefore, we only calculate a single forward projection and add Poisson noise to it. We assumed two detectors, one on each side of the breast. We then show the geometrical mean of the two images from the opposite detectors, as this has been shown to give the best results (Judy *et al* 2010).

2.6. Analysis of images

Besides visually inspecting different images, we compared different breast phantom images by calculating the contrast C of the lesion with respect to the background

$$C = \frac{\bar{S} - \bar{B}}{\bar{B}}. \quad (1)$$

We also determined the contrast-to-noise ratio CNR given by

$$\text{CNR} = \frac{\bar{S} - \bar{B}}{\sigma_B}. \quad (2)$$

In these equations \bar{S} is the average voxel value taken in a circular region with the same diameter as the lesion placed on top of the lesion, \bar{B} is the average signal in a background region, and σ_B is the standard deviation in the background region and serves as measure of the noise. The regions used are shown in figure 4(b).

To get a measure of how contrast varies over different noise realizations, we simulated 20 noise realizations. For reconstructed images such as obtained with MBT, contrast and noise both depend on the number of iterations used and the post-filtering applied while planar MBI images are only affected by the level of post-filtering. We choose to use a constant number of 20 iterations for MBT, and investigate the contrast-to-noise trade-off by applying a progressive series of Gaussian filters (with FWHM from 0 to 10 mm in steps of 1 mm) both for planar MBI and MBT. For each noise realisation, the contrast and noise were determined, and the average of the contrast over the noise realisations was plotted in a contrast versus noise graph.

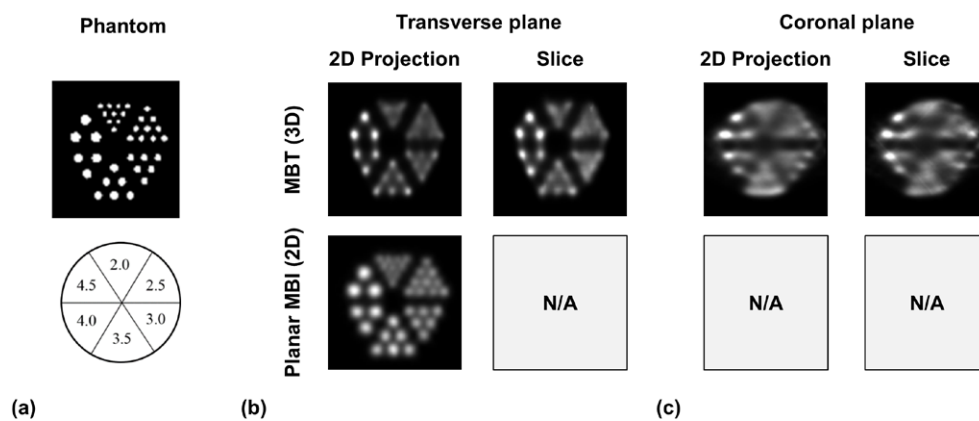


Figure 5. Images of capillary Derenzo resolution phantom. (a) Capillary Derenzo resolution phantom with 40 mm length rods having diameters of 2.0, 2.5, 3.0, 3.5, 4.0 and 4.5 mm. (b) Simulation results for said phantom, where top row is for the MBT system and bottom row is image for planar MBI. First column shows the sum of the reconstructed slices (for MBT and planar MBI), second column shows a slice (only for MBT) through the reconstruction. (c) Similar images as in (b) are shown but not for the phantom placed in the coronal plane. Note that planar MBI cannot provide an image in this plane, due to lack of depth information. Slice thickness was 5 mm.

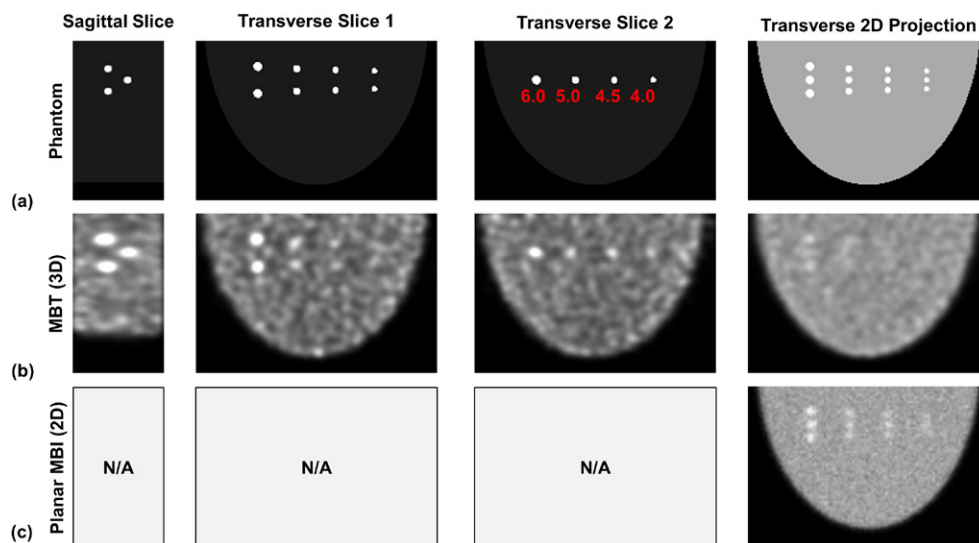


Figure 6. Simulated images of breast shaped phantom containing lesions of 4.0, 4.5, 5.0 and 6.0 mm. (a) Phantom images from left to right: slice parallel to sagittal plane through the lesions, transverse slice at depth of two lesions, transverse slice at depth of third lesion, sum of transverse slices for comparison with planar MBI; all slices are 1.5 mm thick. (b) MBT images in the same representation as in (a), and shown using 4.0 mm FWHM Gaussian filter to match noise in 2D projection to planar MBI. (c) Unfiltered planar MBI image, representing a geometrical mean of two detector images placed at either side of the breast.

As stated in section 3.3, MBT images shown were post-filtered with a 4.0 mm FWHM Gaussian filter. This filter was chosen as it resulted in the same noise level as the planar MBI images that we displayed.

3. Results

3.1. Sensitivity maps and scan sequences

In figure 3(a), we provide a map representing the sensitivity of MBT in sagittal and transverse slices through the breast for one stationary collimator-detector position. The sensitivity map clearly reveals a pattern representing the FOVs of individual pinholes. By moving the collimators and detectors, this pattern is averaged out. Moreover, regions of decreased sensitivity in the FOV of one collimator are sampled by the opposite collimator, although with a relatively low sensitivity. In figures 3(b) and (c), we show the resulting average sensitivity for the FM and the WBM scan sequences tested in this paper. In the WBM, the complete breast is imaged with an almost uniform sensitivity of 0.05%. The FM has 4.1 times higher average sensitivity compared to the WBM in the VOI indicated by the blue dashed box in figure 3(b).

3.2. Resolution phantom

Simulated images of the Derenzo resolution phantom are shown in figure 5. A 2D projection is shown both for MBT (by summing reconstructed slices) and for planar MBI while a slice through the phantom is provided for MBT. For the first scan, the phantom was placed in the transverse plane (i.e. parallel to the collimator plates). With the phantom oriented this way, MBT could resolve 3.0 mm rods (see figure 5(b)) while the planar breast imaging system resolved the 2.5 mm and larger rods (see figure 5(b)).

The phantom was then placed in the coronal plane, for a second scan simulation. From the images, it is clear that MBT can still distinguish the 4.0 mm rods (see figure 5(c)), although we see attenuation artefacts in the centre of the figure. Given the geometry of the collimator (i.e. the limited angular sampling), it was expected to find a poorer depth resolution than the 3.0 mm resolution obtained in the transverse plane. Note that planar MBI systems cannot provide imaging in the depth direction, so one would only be able to get a side view of the phantom.

3.3. Breast shaped phantom

For the breast phantom, simulated images for 10 min scans are provided in figure 6. In figure 6(a), a sagittal slice through the phantom, 2 transverse slices (at the depth of the lesions), and the transverse sum are shown (representing a 2D projection of the breast). Corresponding slices and transverse 2D projection obtained with MBT can be found in figure 6(b). For MBT, we used the WBM sequence for obtaining data. Due to its planar nature, MBI can only provide a 2D projection, which is shown in figure 6(c).

In the 2D projections of the breast obtained with MBT and planar MBI, tumours at different depths appear to have equally strong tracer uptake, which immediately shows the limitation of planar imaging; the difference in depth of the tumours cannot be inferred from a planar scan. All MBT images in figure 6 were filtered with a 3D Gaussian filter with a FWHM of 4.0 mm, resulting in the same noise level as planar MBI for the 2D projections (as explained below). As MBT provides a full 3D reconstruction of the tracer's biodistribution, it allows

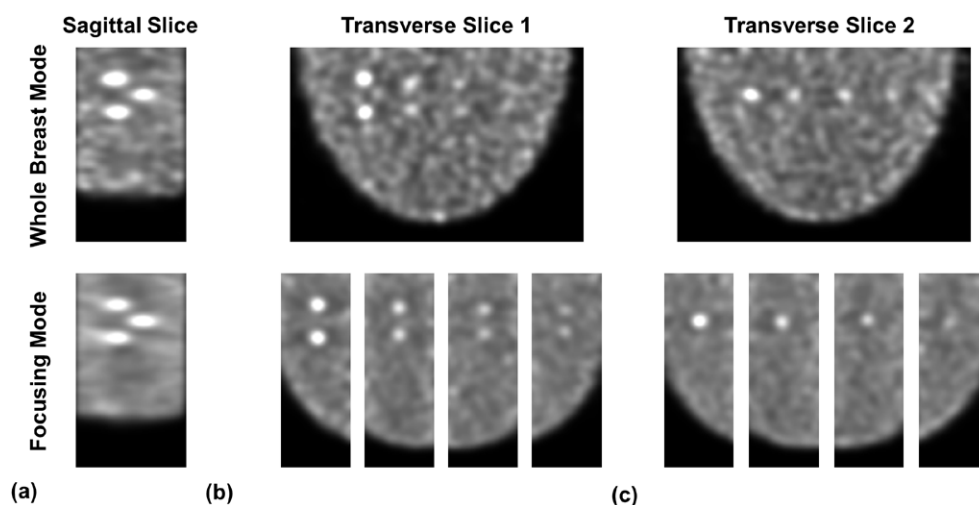


Figure 7. Comparison of WBM and FM of MBT for same digital breast phantom as in figure 6(a). Slices through reconstructed images are shown in (a) sagittal plane and in (b) and (c) transverse plane at 2 different depths.

extracting more information than just a 2D projection. This advantage is clearly illustrated by the slices taken at various depths in the breast phantom and shown in figure 6(b). The slices show that not all three lesions are at the same depth.

A unique property of MBT is the ability to select a patient-dependent scan volume. To analyse the advantage of focusing on a region with known tumours, we also imaged the same phantom with the scan sequence in which we focused on a set of tumours (the FM, VOI is shown in figure 4(a)). Such a focused scan was repeated for each set of tumours in the phantom. In figure 7, we compare images obtained in the FM to those acquired in the WBM. Figure 7(a) shows a sagittal slice through the centre of the breast while transverse slices through the tumours are provided in figures 7(b) and (c).

Profiles through the centre of the 6.0 mm lesions acquired from different images are compared in figure 8 (locations of the profiles are indicated in figure 4(c)). Figure 8(a) compares profiles obtained from 2D projections from MBT (both modes) and planar MBI. From these we see that planar MBI has the highest contrast, but that in the background region the FM results in a smoother profile, i.e. is less noisy than planar MBI and MBT WBM.

Figure 8(b) shows profiles acquired from the MBT slices in figure 7. These profiles show that the availability of different slices does not only allow to obtain depth information but also allows to obtain much better tumour-to-background contrast; in profiles of figure 8(b) tumour signals rise much more above the background than in figure 8(a). From the comparison of profiles from WMB and FM in figure 8(b), one can infer that the FM gives a slightly lower contrast as the WBM, but with a much smoother background, which may ease identification of anomalies.

A more quantitative contrast-to-noise analysis was done for all tumour sizes. In figure 9, the contrast of tumours over the background obtained from different images is plotted against the background noise for each lesion size. Different points in the graph represent a series of progressively more Gaussian filtering. This way, the contrast-noise trade-off can be tuned, and the different contrasts can be compared at equal noise levels. We provide contrast and noise obtained from planar MBI images (figure 6(c)), summed 2D projection images (figure 6(b))

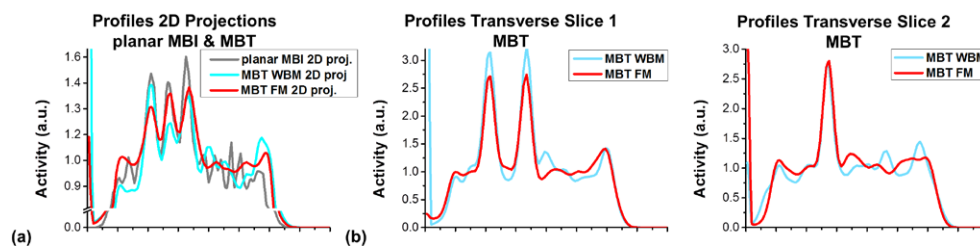


Figure 8. Profiles (1.5 mm wide) through centre of the 6.0 mm lesions obtained from different images. (a) Profiles through transverse 2D projections (figures 6(b), (c) and 7) of planar MBI, MBT WBM and MBT FM. (b) Profiles through transverse slices at 2 different depths comparing MBT in WBM and in FM, from figures 7(b) and (c).

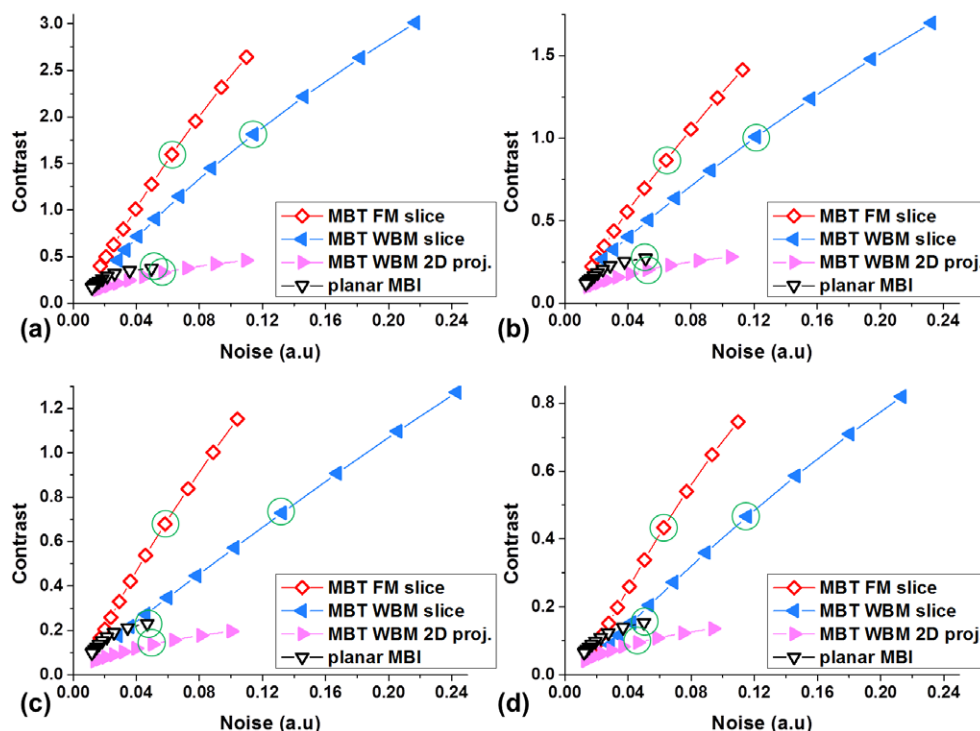


Figure 9. A plot of (a) contrast versus noise for 6.0 mm lesion, points represent different FWHM (range 0.0 to 10 mm, steps 1 mm) of the Gaussian filter. The same contrast-noise plot as in (a) but for (b) 5.0 mm lesion, (c) 4.5 mm lesion, (d) 4.0 mm lesion. The green circles indicate the filter level used in the comparisons in table 1, and plotted images.

and from slices acquired with MBT (figures 6 and 7). This allows analysing if 3D imaging not only offers better tumour localization, but also improves contrast-noise characteristics for tumour scanning.

We see in figure 9, that the line representing the 2D projection for MBT is somewhat below that of planar MBI, i.e. the contrast is lower at an equal noise level as is also clear from the images in figure 6. This changes when tumour-to-background contrast is determined from slices; in that case MBT in WBM has a slightly higher contrast (at equal noise) than planar MBI, while in FM the contrast improvement is much larger (typically a factor 2 over planar MBI).

Table 1. List of contrasts and contrast-to-noise ratios (CNR) obtained for unfiltered planar MBI and images from MBT filtered with 4.0 mm Gaussian (images shown in figures 6 and 7), resulting in equal noise for 2D projections.

Lesion diameter (mm)	Planar		MBT 2D projection WBM		MBT slice WBM		MBT slice FM	
	MBI 2D projection							
	Contrast	CNR	Contrast	CNR	Contrast	CNR	Contrast	CNR
4.0	0.16 ± 33%	3.6 ± 54%	0.10 ± 58% (−39%)	2.1 ± 65% (−42%)	0.47 ± 51% (+201%)	4.0 ± 57% (+12%)	0.43 ± 19% (+180%)	6.9 ± 28% (+92%)
4.5	0.23 ± 15%	5.7 ± 43%	0.14 ± 40% (−40%)	2.7 ± 46% (−52%)	0.73 ± 36% (+218%)	5.5 ± 44% (−3%)	0.68 ± 18% (+196%)	11.7 ± 29% (+105%)
5.0	0.27 ± 13%	6.3 ± 43%	0.20 ± 27 (−25%)	3.9 ± 34% (−38%)	1.01 ± 24% (+268%)	8.3 ± 35% (+33%)	0.87 ± 12% (+217%)	13.5 ± 23% (+115%)
6.0	0.37 ± 8%	7.5 ± 15%	0.33 ± 17% (−12%)	5.8 ± 32% (−23%)	1.81 ± 16% (+386%)	15.8 ± 33% (+111%)	1.60 ± 8% (+328%)	25.6 ± 32% (+241%)

Note: For all numbers the standard deviation over the 20 noise realizations is given. For MBT the difference in contrast and CNR with respect to planar MBI is indicated.

To get an impression of the results that could be obtained for a lower dose, the contrast-noise analysis shown in figure 9 and table 1 were repeated using only 1/4th of the dose used in the paper. Figure A2 and table A1 in the supplementary information (stacks.iop.org/PMB/61/5508/mmedia), which display analogous results to figure 9 and table 1, show that while the CNR is reduced for lower doses both for MBI and MBT the relative performance of MBI and MBT remains similar.

As mentioned above, for the MBT images shown in figures 6 and 7, a 4.0 mm FWHM Gaussian was used as the noise in the 2D projections is then close to the noise in unfiltered planar MBI images. Contrast-noise for these filter settings is indicated with the circles in figure 9 and the contrast and CNR are provided in table 1. From the values in this table, it can be seen that if a transverse sum (2D projection) is generated from MBT images in WBM, MBT achieves a 12–40% lower contrast as planar MBI at equal noise level. However, using slices through reconstructed MBT images can significantly enhance the tumour-to-background contrast, e.g. on average (over all lesions) MBT in WBM has 268% better contrast than the planar MBI image, see table 1. This corresponds with the large contrast improvements shown in the profiles of figure 8. Note that the same amount of activity and equal scan time was used for both planar MBI and for MBT.

While the level of filtering used for the images in figures 6 and 7, and for the results in table 1, was chosen such that the noise level is equal in 2D projections, slices from the MBT reconstructions have different levels of noise than the 2D projections. Therefore, we also provide CNR in table 1. Overall, the slices from MBT provide a significantly higher CNR than planar MBI. In terms of CNR, MBT in WBM performs ~72% better than planar MBI for the larger 5.0 and 6.0 mm lesions, and has no improvement for the smallest 4.0 mm lesions. Here, the use of MBT in FM has a very clear advantage as it can significantly improve CNR, with an increase ranging from 92% for the smallest lesion to 241% for the largest lesion compared to planar MBI.

4. Discussion

In simulations, we compared MBT to planar MBI. For breast tumour imaging, we found that MBT in WBM has up to 111% higher CNR, while a FM achieved up to 241% higher CNR than planar MBI. This large improvement of the contrast-to-noise ratio achieved by focusing on a region containing tumours can be explained by the extra sensitivity it provides in the VOI (see figure 3(b)) which leads to a reduction in the noise while maintaining the contrast. Besides improving tumour CNR over planar MBI, MBT provides information about the depth of a lesion, information that by definition is not available in planar images. Moreover, it may help to better estimate shape and size of the lesion, which is important for determining its possible malignancy. Further evaluation of different imaging scenarios could be of interest for future research.

For this study, we showed MBT images for which the number of MLEM iterations and the Gaussian post filter were tuned such that in the WBM 2D projections (obtained by summing slices from the reconstructed image) have a similar noise level as the planar MBI images. This allows for a comparison between contrast for MBT and planar MBI at the same noise level. Further research will be needed to determine a practical stopping criterion and filter settings for a real patient scanner.

Planar MBI has seen many improvements over the past few years. For the comparison with MBT in this paper, we simulated one of the most recent and best performing system geometries. Although we believe that first results are very promising, this study is only a first introduction of MBT based on multiple pinholes. Even in this stage, MBT already

outperforms planar MBI in terms of CNR and depth information. We believe that MBT can certainly be improved with further research to optimize the design-parameters, such as the collimator-to-detector distance, pinhole-opening angles, amount of focusing etc. This could include optimizing the pinhole layout for scanning the chest wall area. Moreover, we work on ways to eliminate the dead edges of the detector, e.g. using side detectors (Salvador *et al* 2012). In addition, others have proposed ways to reduce dead edges, e.g. by using maximum likelihood processing, smaller PMTs, or PSPMTs etc (Milster *et al* 1985, 1990, Moore *et al* 2007, Barrett *et al* 2009).

Furthermore, future research could include investigating alternative collimators (e.g. fan beam collimators), or different detectors, such as CZT detectors which are already successfully applied in planar MBI. Although a preliminary comparison showed limited benefit when using current CZT detectors, these types of detectors are under active development and may deserve further consideration in the near future.

Besides improving MBT's geometry, it might be valuable to investigate if the use of a prior in image reconstruction is beneficial, i.e. to use Maximum-A-Posteriori reconstruction instead of MLEM. This could improve uniformity in the background. However, the selection of an appropriate prior requires extensive research.

An important issue to be considered in MBI is the dose administered to the patient. After the first introduction of MBI, extensive optimization studies have been conducted to allow for significant dose reduction. To give an indication of how MBT performs when dose is lowered, in the supplementary data we show how contrast and CNR are affected when only a quarter of the dose assumed in this paper is used. This indicates that MBT is not more severely affected by lowering the dose than MBI. In future work, we plan to study in more detail how performance of MBT is affected by dose and we will conduct optimization studies to optimize MBT's performance for lower dose, e.g. by tuning the resolution-sensitivity trade-off by the choice of pinhole diameter.

In this paper, we ignored the time needed for mechanical movement between positions. The mechanical design allows making the very short movements (6 mm) between positions faster than 0.1 s, resulting in a total dead time below 15 s. For a 10 min scan time, we think that the 2.5% extra time needed is negligible. In addition, the dead time could be completely removed when acquisition would be performed in list mode.

Although the comparison of tumour imaging using CNR as a figure of merit favours MBT over planar MBI, this does not necessarily mean that MBT offers superior lesion detectability. Determining detectability is a complicated process influenced by many factors, such as the object and background statistics. The CNR is a measure for how strongly the reconstructed signal rises above the background and its fluctuations. This implies that a higher CNR makes it easier to detect whether the signal is present or not. In future research, we plan to investigate which figures of merit predict how well a system is able to detect tumours. Naturally, one could also consider a comparison based on determining and comparing receiver operating characteristic curves for planar MBI and MBT.

5. Conclusion

In this paper, we have presented a first MBT design based on multiple pinholes and evaluated its performance in a simulation study. From the simulated images, we conclude that our system attains a higher contrast-to-noise ratio for tumours than a planar imaging system. This might lead to better lesion detection and identification. Furthermore, the ability to recover depth information can be of great additional value.

In addition, MBT can focus on a suspected lesion or region. The FM was shown to reduce background noise compared to whole breast imaging, while maintaining the contrast. This may improve lesion detection, but could also reduce the scan time while producing similar images as with whole breast imaging. We conclude that MBT might be a promising approach that can fill a niche in the breast-imaging field.

Acknowledgments

This work is supported by the Dutch Organization for Scientific Research (NWO) under the VIDI grant 'Focused imaging of tumors'. The authors would like to thank Oleksandra Ivashchenko for the illustrations of the breasts in figure 2. Moreover, the authors would like to thank Beien Wang for providing the GATE simulations.

References

- Barrett H H, Hunter W C J, Miller B W, Moore S K, Yichun C and Furenlid L R 2009 Maximum-likelihood methods for processing signals from gamma-ray detectors *IEEE Trans. Nucl. Sci.* **56** 725–35
- Beekman F and van der Have F 2007 The pinhole: gateway to ultra-high-resolution three-dimensional radionuclide imaging *Eur. J. Nucl. Med. Mol. Imaging* **34** 151–61
- Beekman F J 2011 Gamma radiation imaging apparatus *US Patent* 20110158384, EP 2310876
- Beekman F J 2014 Gamma radiation breast imaging apparatus *US Patent* 20140093035, NL 2009566
- Beekman F J, van der Have F, Vastenhouw B, van der Linden A J, van Rijk P P, Burbach J P and Smidt M P 2005 U-SPECT-I: a novel system for submillimeter-resolution tomography with radiolabeled molecules in mice *J. Nucl. Med.* **46** 1194–200
- Branderhorst W et al 2014 Three-dimensional histologic validation of high-resolution SPECT of antibody distributions within xenografts *J. Nucl. Med.* **55** 830–7
- Branderhorst W, Vastenhouw B, van der Have F, Blezer E A, Bleeker W and Beekman F 2011 Targeted multi-pinhole SPECT *Eur. J. Nucl. Med. Mol. Imaging* **38** 552–61
- Brem R F, Floerke A C, Rapelyea J A, Teal C, Kelly T and Mathur V 2008 Breast-specific gamma imaging as an adjunct imaging modality for the diagnosis of breast cancer *Radiology* **247** 651–7
- Carney P A et al 2003 Individual and combined effects of age, breast density, and hormone replacement therapy use on the accuracy of screening mammography *Ann. Int. Med.* **138** 168–75
- Dickerscheid D, Lavalaye J, Romijn L and Habraken J 2013 Contrast-noise-ratio (CNR) analysis and optimisation of breast-specific gamma imaging (BSGI) acquisition protocols *EJNMMI Res.* **3** 1–9
- Dong S-L, Chu T-C, Lan G-Y, Lin Y-C, Yeh Y-H and Chuang K-S 2011 Development of an adjustable model breast for mammographic dosimetry assessment in Taiwanese women *Am. J. Roentgenol.* **196** W476–81
- Fowler A M 2014 A molecular approach to breast imaging *J. Nucl. Med.* **55** 177–80
- Gong Z and Williams M B 2015 Comparison of breast specific gamma imaging and molecular breast tomosynthesis in breast cancer detection: evaluation in phantoms *Med. Phys.* **42** 4250–9
- Goorden M, van Roosmalen J, van der Have F and Beekman F 2016 Optimizing modelling in iterative image reconstruction for preclinical pinhole PET *Phys. Med. Biol.* **61** 3712–33
- Gopan O, Gilland D, Weisenberger A, Kross B and Welch B 2014 Molecular imaging of the breast using a variable-angle slant-hole collimator *IEEE Trans. Nucl. Sci.* **61** 1143–52
- Harris C H 2010 New imaging tools address challenges of dense breast tissue *AuntMinnie.com Special Report: Advances in MBI* <http://www.auntminnie.com/index.aspx?sec=spt&sub=mbi&pag=dis&temID=91901>
- Helvie M A, Chan H P, Adler D D and Boyd P G 1994 Breast thickness in routine mammograms: effect on image quality and radiation dose *Am. J. Roentgenol.* **163** 1371–4
- Hruska C B and O'Connor M K 2006 CZT detectors: how important is energy resolution for nuclear breast imaging? *Phys. Medica* **21** 72–5
- Hruska C B and O'Connor M K 2008a A Monte Carlo model for energy spectra analysis in dedicated nuclear breast imaging *IEEE Trans. Nucl. Sci.* **55** 491–500

- Hruska C B and O'Connor M K 2008b Quantification of lesion size, depth, and uptake using a dual-head molecular breast imaging system *Med. Phys.* **35** 1365–76
- Hruska C B and O'Connor M K 2013 Nuclear imaging of the breast: translating achievements in instrumentation into clinical use *Med. Phys.* **40** 050901
- Hruska C B, Phillips S W, Whaley D H, Rhodes D J and O'Connor M K 2008 Molecular breast imaging: use of a dual-head dedicated gamma camera to detect small breast tumors *Am. J. Roentgenol.* **191** 1805–15
- Hruska C B, Weinmann A L and O'Connor M K 2012a Proof of concept for low-dose molecular breast imaging with a dual-head CZT gamma camera. Part I. Evaluation in phantoms *Med. Phys.* **39** 3466–75
- Hruska C B, Weinmann A L, Skjerseth C M T, Wagenaar E M, Conners A L, Tortorelli C L, Maxwell R W, Rhodes D J and O'Connor M K 2012b Proof of concept for low-dose molecular breast imaging with a dual-head CZT gamma camera. Part II. Evaluation in patients *Med. Phys.* **39** 3476–83
- Ivashchenko O, van der Have F, Villena J L, Groen H C, Ramakers R M, Weinans H H and Beekman F J 2014 Quarter-millimeter-resolution molecular mouse imaging with U-SPECT *Mol. Imaging* **13** 1–8
- Jan S *et al* 2004 GATE: a simulation toolkit for PET and SPECT *Phys. Med. Biol.* **49** 4543
- Jan S *et al* 2011 GATE V6: a major enhancement of the GATE simulation platform enabling modelling of CT and radiotherapy *Phys. Med. Biol.* **56** 881
- Judy P G *et al* 2010 Analysis of image combination methods for conjugate breast scintigraphy *IEEE Trans. Nucl. Sci.* **57** 1146–54
- Kolb T M, Lichy J and Newhouse J H 2002 Comparison of the performance of screening mammography, physical examination, and breast US and evaluation of factors that influence them: an analysis of 27 825 patient evaluations *Radiology* **225** 165–75
- Lång K, Andersson I, Rosso A, Tingberg A, Timberg P and Zackrisson S 2016 Performance of one-view breast tomosynthesis as a stand-alone breast cancer screening modality: results from the Malmö breast tomosynthesis screening trial, a population-based study *Eur. Radiol.* **26** 184
- Lee C H *et al* 2010 Breast cancer screening with imaging: recommendations from the society of breast imaging and the ACR on the use of mammography, breast MRI, breast ultrasound, and other technologies for the detection of clinically occult breast cancer *J. Am. Col. Radiol.* **7** 18–27
- Lee T, Braun K, Jaszczak R, Bowsher J and Bobkov K 2004 The effects of lead shielding of background organ activity in pinhole single photon emission computed tomography (SPECT) breast tumor imaging *Nuclear Science. Symp. Conf. Record* vol 5 pp 3352–6
- Madhav P, Crotty D J, McKinley R L and Tornai M P 2006 Initial development of a dual-modality SPECT-CT system for dedicated mammotomography *Nuclear Science Symp. Conf. Record* vol 4 pp 2382–6
- Mankoff D A, O'Sullivan F, Barlow W E and Krohn K A 2007 Molecular imaging research in the outcomes era: measuring outcomes for individualized cancer therapy *Acad. Radiol.* **14** 398–405
- Mann S D, Perez K L, McCracken E K, Shah J P, Wong T Z and Tornai M P 2012 Initial *in vivo* quantification of Tc-99m Sestamibi uptake as a function of tissue type in healthy breasts using dedicated breast SPECT-CT *J. Oncol.* **2012** 146943
- Maublant J *et al* 1996 Technetium-99m-sestamibi uptake in breast tumor and associated lymph nodes *J. Nucl. Med.* **37** 922–5
- Milster T D, Aarsvold J N, Barrett H H, Landesman A L, Mar L S, Patton D D, Roney T J, Rowe R K and Seacat R H 1990 A full-field modular gamma camera *J. Nucl. Med.* **31** 632–9
- Milster T D, Selberg L A, Barrett H H, Landesman A L and Seacat R H 1985 Digital position estimation for the modular scintillation camera *IEEE Trans. Nucl. Sci.* **32** 748–52
- Miyake K K *et al* 2014 Performance evaluation of a new dedicated breast PET scanner using NEMA NU4-2008 standards *J. Nucl. Med.* **55** 1198–203
- Mok G S P, Yuchuan W and Tsui B M W 2009 Quantification of the multiplexing effects in multi-pinhole small animal SPECT: a simulation study *IEEE Trans. Nucl. Sci.* **56** 2636–43
- Moore S K, Hunter W C J, Furenlid L R and Barrett H H 2007 Maximum-likelihood estimation of 3D event position in monolithic scintillation crystals: experimental results *Nuclear Science Symp. Conf. Record* vol 5 pp 3691–4
- O'Connor M, Rhodes D, Hruska C, Phillips S and Whaley D 2008 Molecular breast imaging (MBI) as an adjunct to screening mammography *J. Nucl. Med.* **49** 40 P
- O'Connor M K, Phillips S W, Hruska C B, Rhodes D J and Collins D A 2007 Molecular breast imaging: advantages and limitations of a scintimammographic technique in patients with small breast tumors *Breast J.* **13** 3–11

- Orlov S 1975 Theory of three dimensional reconstruction: I. Conditions for a complete set of projections *Sov. Phys. Crystallogr.* **20** 312–4
- Perez K L, Cutler S J, Madhav P and Tornai M P 2010 Characterizing the contribution of cardiac and hepatic uptake in dedicated breast SPECT using tilted trajectories *Phys. Med. Biol.* **55** 4721
- Perez K L, Cutler S J, Madhav P and Tornai M P 2011 Towards quantification of functional breast images using dedicated SPECT with non-traditional acquisition trajectories *IEEE Trans. Nucl. Sci.* **58** 2219–25
- Peterson T E and Furenlid L R 2011 SPECT detectors: the anger camera and beyond *Phys. Med. Biol.* **56** R145
- Peterson T E and Shokouhi S 2012 Advances in preclinical SPECT instrumentation *J. Nucl. Med.* **53** 841–4
- Pisano E D et al 2008 Diagnostic accuracy of digital versus film mammography: exploratory analysis of selected population subgroups in DMIST *Radiology* **246** 376–83
- Rhodes D J, O'Connor M K, Phillips S W, Smith R L and Collins D A 2005 Molecular breast imaging: a new technique using technetium Tc 99m scintimammography to detect small tumors of the breast *Mayo Clin. Proc.* **80** 24–30
- Salvador S, Korevaar M A N, Heemskerk J W T, Kreuger R, Huizenga J, Seifert S, Schaart D R and Beekman F J 2012 Improved EMCCD gamma camera performance by SiPM pre-localization *Phys. Med. Biol.* **57** 7709
- Scopinaro F, Pani R, De Vincentis G, Soluri A, Pellegrini R and Porfiri L M 1999 High-resolution scintimammography improves the accuracy of technetium-99m methoxyisobutylisonitrile scintimammography: use of a new dedicated gamma camera *Eur. J. Nucl. Med.* **26** 1279–88
- Sechopoulos I 2013 A review of breast tomosynthesis. Part I. The image acquisition process *Med. Phys.* **40** 014301
- Segars W P, Sturgeon G, Mendonca S, Grimes J and Tsui B M W 2010 4 D XCAT phantom for multimodality imaging research *Med. Phys.* **37** 4902–15
- Segars W P and Tsui B M W 2009 MCAT to XCAT: the evolution of 4D computerized phantoms for imaging research *Proc. IEEE* **97** 1954–68
- Skaane P et al 2013 Comparison of digital mammography alone and digital mammography plus tomosynthesis in a population-based screening program *Radiology* **267** 47–56
- Sullivan D C, Beam C A, Goodman S M and Watt D L 1991 Measurement of force applied during mammography *Radiology* **181** 355–7
- Sullivan O, Gong Z, Klanian K, Patel T and Williams M 2012 *Breast Imaging* ed A A Maidment et al (Berlin: Springer) pp 300–7
- Sun Y, Wei W, Yang H-W and Liu J-L 2013 Clinical usefulness of breast-specific gamma imaging as an adjunct modality to mammography for diagnosis of breast cancer: a systemic review and meta-analysis *Eur. J. Nucl. Med. Mol. Imag.* **40** 450–63
- Tuy H K 1983 An inversion formula for cone-beam reconstruction *SIAM J. Appl. Math.* **43** 546–52
- Vaissier P E B, Goorden M C, Vastenhouw B, van der Have F, Ramakers R M and Beekman F J 2012 Fast spiral SPECT with stationary γ -cameras and focusing pinholes *J. Nucl. Med.* **53** 1292–9
- van der Have F, Vastenhouw B, Ramakers R M, Branderhorst W, Krah J O, Ji C, Staelens S G and Beekman F J 2009 U-SPECT-II: an ultra-high-resolution device for molecular small-animal imaging *J. Nucl. Med.* **50** 599–605
- van Roosmalen J, Goorden M C and Beekman F J 2015 Optimization of a high resolution focussed molecular breast tomosynthesis device *IEEE Nuclear Science Symposium and Medical Imaging Conf. (NSS/MIC)*, 2015
- Vastenhouw B and Beekman F 2007 Submillimeter total-body murine imaging with U-SPECT-I *J. Nucl. Med.* **48** 487–93
- Vunckx K, Suetens P and Nuyts J 2008 Effect of overlapping projections on reconstruction image quality in multipinhole SPECT *IEEE Trans. Med. Imag.* **27** 972–83
- Wackers F J T et al 1989 Technetium-99m hexakis 2-methoxyisobutyl isonitrile: human biodistribution, dosimetry, safety, and preliminary comparison to thallium-201 for myocardial perfusion imaging *J. Nucl. Med.* **30** 301–11
- Wang B, van Roosmalen J, Goorden M and Beekman F 2016 Fast and accurate ray-tracing simulation of multi-pinhole molecular breast tomosynthesis *Society of Nuclear Medicine and Molecular Imaging Annual Meeting* accepted
- Wang H, Scarfone C, Greer K L, Coleman R E and Jaszczak R J 1996 Prone breast tumor imaging using vertical axis-of-rotation (VAOR) SPECT systems: an initial study *Nuclear Science Symp. Conf. Record* vol 2 pp 1387–91
- Weinmann A L, Hruska C B and O'Connor M K 2009 Design of optimal collimation for dedicated molecular breast imaging systems *Med. Phys.* **36** 845–56
- Williams M B, Judy P G, Gunn S and Majewski S 2010 Dual-modality breast tomosynthesis *Radiology* **255** 191–8